Enhanced photocatalytic degradation of bisphenol A by Co-doped BiOCl nanosheets under visible light irradiation

Chu-Ya Wang, Ying-Jie Zhang, Wei-Kang Wang, Dan-Ni Pei, Gui-Xiang Huang, Jie-Jie Chen, Xing Zhang[*], Han-Qing Yu[*]

CAS Key Laboratory of Urban Pollutant Conversion, Department of Chemistry, University of Science & Technology of China, Hefei, 230026, China

A B S T R A C T

Bismuth oxychloride (BiOCl) is a typical UV-light-sensitive photocatalyst with a unique layered structure, but exhibits no response towards visible light. This is a main limitation for its practical applications in photocatalytic degradation of pollutants. Among various methods to expand the light absorption region, doping modification is an efficient approach because it can tailor the band structure by forming a doping energy level without changing the layered structure substantially. In this case, the static electric field in the BiOCl crystal can be retained. Since cobalt (Co) exhibits good electrochemical properties, it is an ideal element for doping modification to expand the light absorption region and enhance the charge separation efficiency of BiOCl. In this work, Co-doped BiOCl nanosheets were prepared using a simple hydrothermal route. The doped Co expanded the light absorption region and enhanced the charge separation efficiency by forming a doping energy level in the band gap of BiOCl. As a result, the Co-BiOCl nanosheets exhibited an outstanding photocatalytic performance in degrading bisphenol A (BPA) under visible light irradiation with a degradation rate of 3.5 times higher than that of BiOCl. On the basis of the experimental results and density functional theory calculations, the mechanism of visible-light-driven catalytic BPA degradation by the Co-BiOCl nanosheets was elucidated. Therefore, the feasibility of Co-doping modification for BiOCl was confirmed, and a novel and efficient strategy was provided for the design and synthesis of high-performance photocatalysts.

1. Introduction

Photocatalysis is recognized as an efficient technology for water purification using solar energy and has attracted extensive interests in recent years [1–4]. Among various photocatalysts, bismuth oxychloride (BiOCl) possesses a unique layered structure, in which a $[Bi_2O_2]^{2+}$ layer is sandwiched by two $[Cl_2]^{2-}$ layers in the crystal [5–7]. As a result, the static electric field perpendicular to $[Bi_2O_2]^{2+}$ and $[Cl_2]^{2-}$ layers caused by the difference in electronegativities can induce the separation of photogenerated electron-hole (e^--h^+) pairs, which contributes to a good photocatalytic activity [8–10]. Although BiOCl has been reported to be able to degrade some organic dyes under visible light irradiation with the help of dye-sensitization, BiOCl is a typical UV-light-driven photocatalyst with a wide band gap of approximately 3.4 eV but shows no responses towards visible light, which is dominant in solar light [11–13]. Since most organic pollutants are non-dye molecules, BiOCl is helpless to fight against these colorless pollutants under visible light irradiation. This has become a main limitation for its practical application [14]. Therefore, a simple and efficient

modification method for BiOCl is highly desired to achieve a remarkable photocatalytic activity without dye-sensitization under visible light irradiation.

So far, many efforts have been made to improve the light absorption property of BiOCl. Our previous works show that coupling BiOCl and BiOBr to form a solid solution of $BiOCl_xBr_{1-x}$ and oxygen-rich modification of BiOCl to form $Bi_{12}O_{15}Cl_6$ and $Bi_{12}O_{17}Cl_2$ are effective ways to enhance the photocatalytic performance of BiOCl under visible light irradiation [15–17]. Furthermore, introduction of oxygen vacancies as lattice defects, formation of Schottky junctions with metallic elementary substances and tailoring the size, morphology or exposed facets have also been tried to make BiOCl a visible-light-responsive photocatalyst [9,18–23]. However, several drawbacks still remain to be overcome. For example, tailoring morphology does not change the intrinsic light absorption property of BiOCl, forming heterojunction is difficult to obtain a highly homogeneous distribution, and changing phase may destroy the layered structure and thus weaken the contribution of the static electric field in BiOCl crystals [24–27].

Doping modification is an effective strategy as it affects the band

* Corresponding authors.
  E-mail addresses: zhx0610@ustc.edu.cn (X. Zhang), hqyu@ustc.edu.cn (H.-Q. Yu).

structure by forming a doping energy level without changing the host crystal structure substantially [28–31]. It has been reported that the doped Fe element could narrow the band gap of BiOCl nanosheets and activate the photogenerated H_2O_2, and thus enhanced the photocatalytic performance of BiOCl [32]. Moreover, C-doping modification of BiOCl could also achieve response towards visible light [33]. Inspired by these works, we assume that cobalt (Co) should be another promising element to be doped into BiOCl, which has not been reported yet. Since Co exhibits good electrochemical properties, the light absorption region of BiOCl might be expanded and the charge separation efficiency is also probable to be enhanced by doping Co element [34–36].

Therefore, in this work, Co-BiOCl nanosheets were synthesized via a simple hydrothermal route for the first time. The as-prepared Co-BiOCl nanosheets were characterized systematically by various techniques. More importantly, the role of doped Co element was evaluated in terms of light absorption, charge separation and charge injection. Additionally, density functional theoretical (DFT) calculation was also performed to further demonstrate the impact of Co doping on the modification of the energy band structure. In order to verify the feasibility for practical applications, bisphenol A (BPA), a typical non-dye endocrine disrupter in environments, was chosen as the target pollutant to examine the photocatalytic activity of the Co-BiOCl nanosheets under visible light irradiation. The active species responsible for the degradation of BPA over the Co-BiOCl nanosheets was detected, and a BPA degradation pathway was found out. In this way, an efficient strategy for the design and synthesis of high-performance visible-light-sensitive photocatalysts was proposed.

2. Experimental section

2.1. Synthesis of Co-BiOCl nanosheets

All chemicals used in this work were analytical-grade reagents and purchased from Shanghai Chemical Reagent Co., China. They were used without any further purification. In a typical synthesis procedure of Co-BiOCl nanosheets, 0.485 g of $Bi(NO_3)_3$•$5H_2O$ (1 mmol) and 0.5 mL of Triton X-100 were added into 15 mL of ethylene glycol (EG). After being vigorously stirred and sonicated for 30 min, the mixture became homogeneous and colorless. On the other hand, 0.0238 g of $CoCl_2$ (0.1 mmol), 0.117 g of NaCl (2 mmol) and 0.546 g of mannitol (3 mmol) were added into 15 mL of distilled water under vigorous stirring for several minutes until a homogeneous solution was formed. Then, these two solutions were mixed with vigorous stirring and an obvious suspension was formed immediately. The suspension was kept stirring for another 15 min to insure the sufficient mixing of all these reactants. After that, the suspension was transferred into a 50-mL autoclave with Teflon linear and heated at 160 °C for 12 h. After naturally cooling to room temperature, the resulting solid powders were collected through centrifugation and respectively washed with distilled water and alcohol for three times to remove the residual ions and organics. Finally, the product was dried at 70 °C in vacuum for 12 h prior to characterization. For comparison, BiOCl was also prepared using the same procedure without the utilization of $CoCl_2$.

2.2. Physicochemical characterization

The X-ray powder diffraction (XRD) measurement of the samples was performed using a Philips X' Pert PRO SUPER diffractometer equipped with graphite monochromatized Cu Kα radiation (λ = 1.541874 Å). The inductive coupled plasma (ICP) emission spectrometer (Optima 7300 DV, PerkinElmer Co., USA) was used to determine the doping amount of Co element. Scanning electron microscopy (SEM) images were taken with an X-650 scanning electron micro analyzer and a JSM-6700F field emission SEM (JEOL Co., Japan). Transmission electron microscopy (TEM) (JEM-2011, JEOL Co., Japan)

and high-resolution transmission electron microscopy (HRTEM) (JEOL-2010, JEOL Co., Japan) analyses were performed to characterize the morphology and crystal structure of the samples, and the applied acceleration voltages of TEM and HRTEM were both 200 kV. Additionally, in order to find out the distribution of each element in the products, energy dispersive spectrometer (EDS) spectrum and the EDS mapping image were obtained using TEM and HRTEM, respectively. The surface areas were measured using a Builder 4200 instrument (Tristar II 3020 M, Micromeritics Co., USA) with the Brunauer-Emmett-Teller (BET) method. The X-ray photoelectron spectroscopy (XPS) (ESCALAB250, Thermo Fisher Inc., USA) was used to investigate the chemical compositions and the valence states of constituent elements. The diffuse reflectance spectra (DRS) were measured using a UV/Vis/NIR spectrophotometer (Solid 3700, Shimadzu Co., Japan). The inductively coupled plasma emission spectrometer (ICP) (Optima 7300 DV, Perkin-Elmer Co., USA) was used to measure the amount of doped Co. Raman spectra were obtained using a Raman spectrometer (LabRAM HR Evolution, Horiba Instruments Inc., USA) with a 633 nm laser at ambient temperature.

2.3. Electrochemical characterization

All electrochemical measurements were carried out using a home-made three-electrode system, and the Ag/AgCl (KCl, 3 M) and the Pt wire were used as the reference electrode and the counter electrode, respectively. The sample on glass carbon was used as the working electrode for Mott-Schottky plots determination and electrochemical impedance spectroscopy (EIS) analysis, and the sample on F doped SnO_2 (FTO) conductive glass was as the working electrode for the photocurrent test. In this work, EIS analysis was performed by applying an alternating current (AC) voltage amplitude of 5 mV in 0.5 M K_3[Fe $(CN)_6$] and K_4[Fe$(CN)_6$] aqueous solution within a frequency range from 10^6 to 10^{-2} Hz. Mott-Schottky plots were obtained in 0.1 M Na_2SO_4 aqueous solution by impedance measurement at a fixed frequency of 1 kHz between the applied voltage range of 0-1.0 V (vs Ag/AgCl). The photocurrent responses of the samplse in 0.1 M Na_2SO_4 aqueous solution with or without 0.1 M $K_2S_2O_8$ were determined by amperometric i–t curve measurement with a bias voltage of 0.2 V (the open-circuit voltage of the samples) for 850 s. All these experiments were conducted using a computer-controlled potentiostat (CHI 660E, CH Instrument Co., China) with a three-electrode glass electrochemical cell. The light source applied in the photocurrent measurement was the same as that used in photocatalytic measurements with a UV filter, which is shown in the following section.

2.4. Photocatalytic performance evaluation

The photocatalytic activity of the samples for the BPA degradation was evaluated using a 500 W Xe arc lamp with a 420 nm cutoff filter as the light source at ambient temperature, and the measured radiation flux was approximately 85 mW cm^{-2}. In a typical procedure, 20 mg of the powder as a photocatalyst was added into 30 mL aqueous solution containing 10 mg L^{-1} of BPA. Then, the mixture was sonicated and vigorously stirred in dark for approximately 60 min to ensure sufficient adsorption/desorption equilibrium. After that, the mixture was continuously stirred under light irradiation and the samples were collected at given time intervals. The BPA concentration was measured using a high performance liquid chromatography (HPLC) (1260 Infinity, Agilent Inc., USA) with an Agilent Eclipse XDB-C18 column (4.6 × 150 mm), and the column temperature was 30 °C. Additionally, 50% acetonitrile and 50% deionized water (containing 0.1% formic acid) were used as the mobile phase at a flow rate of 1.0 mL min^{-1}, and the detection wavelength was 273 nm. Furthermore, the electron spin resonance (ESR) (JES-FA200, JEOL Co., Japan) was used to detect reactive radicals. The fluorescence emission spectra were obtained on a fluorescence spectrophotometer (Aqualog-C, Horiba Instruments Inc.,

USA). The gas chromatography-mass spectrometry (GC-MS) (7890 B GC System and 5977 B MDS, Agilent Co., USA) was used to determine the intermediate products from the BPA degradation.

2.5. DFT calculations

The crystal structure of BiOCl was characterized by XRD phase analysis as P4/nmm S1 tetragonal space group and showed a layered structure of $[Bi_2O_2]^{2+}$ slabs interleaved with double slabs of $[Cl_2]^{2-}$ [37]. In this work, periodic surface slab models were constructed for (001) surface of both BiOCl and Co-BiOCl (**Fig. S1**). A Bi atom was substituted by a Co atom on the (001) surface as the model of Co-BiOCl. First-principles calculations were carried out with the periodic plane-wave-ultrasoft pseudopotential method in the CASTEP code [38], and the exchange-correlation effects were described by Perdew-Burke-Ern-zerhof (PBE) functional using the generalized gradient approximation (GGA) [39]. For the geometry optimization process, the Broyden-Fletcher-Goldfarb-Shanno (BFGS) minimization algorithm was adopted and the atoms in all models with 2×2 supercell were fully relaxed with the cut-off energy of 300 eV and k-points of $2 \times 2 \times 1$. The energy and force converged to 2×10^{-5} eV atom^{-1} and 0.05 eV Å^{-1}, respectively. For the subsequent electronic structure calculations, the GGA + U approach was used for Co-BiOCl with the defined U value of Co at 2.5 eV, and the cut-off energy and the k-points increased to 340 eV and $5 \times 5 \times 1$, respectively.

3. Results and discussion

3.1. Characteristics of Co-BiOCl nanosheets

The matter phase of the product was examined on the basis of the powder XRD result (Fig. 1). All the diffraction peaks of the as-prepared product could be indexed to tetragonal BiOCl (JCPDS card No. 06-0249), indicating that the unique layered structure was retained after Co-doping modification. However, no diffraction peaks of any other phases containing Co element were observed, suggesting that the doped Co was highly dispersed and uncrystallized in the BiOCl crystals. Thus, the ICP test of the product was carried out to verify the presence of Co element. The result shows that the molar ratio of Co:Bi was approximately 1:85, indicating that Co element was really introduced into the crystal of the as-prepared BiOCl. Moreover, a comparison between the XRD pattern of the as-prepared Co-BiOCl sample with the corresponding standard card shows that all diffraction peaks shifted to high angles by approximately 0.2°, indicating that the lattice parameters of Co-BiOCl were less than those of BiOCl. Since the atomic radius of Co is smaller than that of Bi, it is convincing that Bi-site atoms in the host crystal were partially substituted by Co atoms, resulting in the change of lattice parameters and the shift of diffraction peak to high angles. Additionally, the (001) peak at 11.9° is attributed to the periodic

Fig. 1. XRD pattern of the as-prepared Co-BiOCl sample.

stacking structure among [Cl-Bi-O-Bi-O-Cl] layers along the c-axis, and the peak at 32.4° belongs to the (110) plane, which is perpendicular to (001) plane [26]. The (110) peak is strong, while the (001) peak is very weak, indicating that the product crystal orientated grew along [110] direction. As a result, (110) facets were suppressed and (001) facets were highly exposed.

The SEM and TEM images were used to observe the morphology of the as-prepared product (Fig. 2). The SEM images (Fig. 2a and b) show that the as-prepared product possessed a large scale sheet-like morphology and the mean size of these nanosheets was approximately 50–100 nm. The TEM image (Fig. 2c) further confirms the two-dimensional sheet-like structure of the product, and the mean thickness was measured as 10–20 nm. Thus, the as-prepared Co-BiOCl nanomaterial exhibited a well uniformed sheet-like morphology. As shown in **Fig. S2**, the morphology of Co-BiOCl nanosheets was similar to that of BiOCl, but the mean size of Co-BiOCl nanosheets was smaller. Moreover, the EDS spectrum of the prepared Co-BiOCl nanosheets was obtained using the TEM (Fig. 2d). The signals of Bi, O and Cl in the EDS spectrum were very strong, indicating that Bi, O and Cl were the main elements in the product. However, a weak signal of Co was also present in the EDS spectrum, re-confirming that the doping of Co element into the as-prepared BiOCl nanosheets. Except Cu and C, no signals of any other elements were observed, indicating the purity of the as-prepared Co-BiOCl nanosheets. Additionally, considering that the surface area is an important factor in photocatalysis, the surface areas of both Co-BiOCl and BiOCl were measured using the BET method, and were calculated as 17.1 and 8.6 m^2 g^{-1} for Co-BiOCl and BiOCl, respectively (**Fig. S3**), suggesting that the surface area of the prepared product was not changed substantially by the Co-doping modification.

The crystal structure of the as-prepared Co-BiOCl nanosheets was further characterized using HRTEM (Fig. 3). Fig. 3a clearly reveals the square shaped structure of the as-prepared Co-BiOCl nanosheets. Fig. 3b, which was taken from the edge of a single Co-BiOCl nanosheet noted in Fig. 3a, reveals a high crystallinity and clear lattice fringes of the Co-BiOCl nanosheets. The continuous lattice fringes with an interplanar lattice spacing of 0.29 nm and an angle of 90° matched well with the (110) atomic planes of tetragonal BiOCl (JCPDS card No. 06-0249). The corresponding SAED pattern (**insert in** Fig. 3b) shows a single-crystalline nature of the BiOCl nanosheets with an angle of 90°, which is in correspondence with the angle between the (110) and (1-10) planes. The diffraction signal of (200) planes was also present, which is noted in the SAED pattern. Thus, the set of diffraction spots could be assigned to the [001] zone axis of tetragonal BiOCl nanosheets, indicating the high exposure of (001) facet. Additionally, the EDS mapping images (Fig. 3c) shows a highly homogeneous distribution of Bi, O and Cl elements in the as-prepared product, and Co element also possessed a homogeneous distribution despite of its very low amount.

The XPS analysis was performed to explore the surface composition and the chemical state of the as-prepared Co-BiOCl and BiOCl (Fig. 4). The peaks of Bi, O, Cl and C could be clearly identified in the full scan spectra of the Co-BiOCl and BiOCl (Fig. 4a), and all of these XPS spectra were corrected for specimen charging by referencing the C 1 s peak to 284.60 eV. In Fig. 4b, Bi 4f XPS spectra show two strong peaks with the splitting energy $\Delta = 5.4$ eV, which could be assigned to the Bi 4f$_{7/2}$ and Bi 4f$_{5/2}$ of Bi^{3+}, respectively [40]. The Bi 4f peaks of Co-doped BiOCl shifted towards a high binding energy than that of BiOCl. As aforementioned, the lattice parameters of Co-BiOCl were reduced by Co-doping modification, indicating that Bi atoms in Co-BiOCl were more close to O atoms. Since the electronegativity of O is much higher than that of Bi, the reduced distance of Bi and O resulted in the high-energy shift of Bi 4f peaks of Co-BiOCl. In the O 1 s XPS spectra (Fig. 4c), the peaks at approximately 530 eV belong to O^{2-} from a bismuth-oxygen bond [17], and the additional peaks at about 533 eV belong to oxygen vacancies in both Co-BiOCl and BiOCl [41]. The Cl 2p XPS spectra (Fig. 4d) obviously exhibit two main peaks with the splitting energy $\Delta = 4.4$ eV, which is in correspondence with the Cl 2p$_{3/2}$ and Cl 2p$_{1/2}$
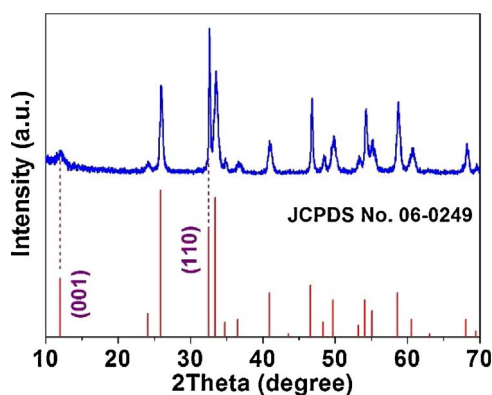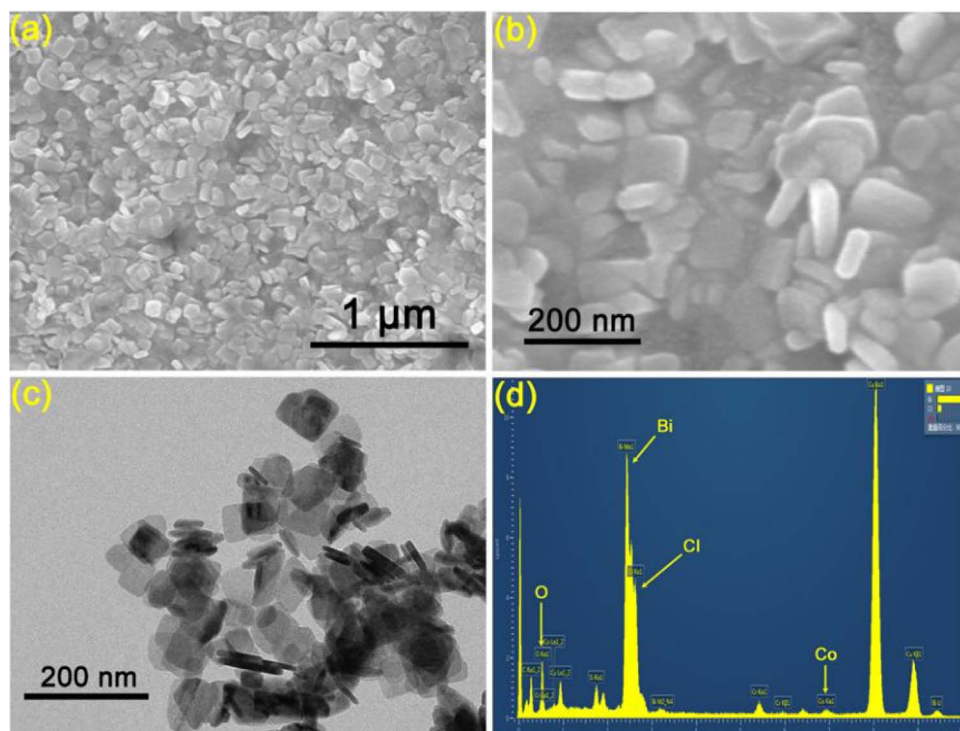
Fig. 2. (a, b) SEM images, (c) TEM image, and (d) EDS spectrum of the as-prepared Co-BiOCl nanosheet.

of Cl, respectively [16]. When it comes to Co (Fig. 4e), no signal appears in the spectrum of the BiOCl sample. However, two weak peaks with the splitting energy $\Delta = 15.5$ eV occur in the spectrum of the Co-BiOCl sample, indicating that the doped Co was in contact with O and formed Co-O bonds in the crystal of the Co-BiOCl nanosheets [42,43]. Furthermore, the valence band (VB) top of the Co-BiOCl and BiOCl were also measured from the XPS VB spectra (Fig. 4f). The VB top positions of the as-prepared Co-BiOCl and BiOCl were calculated as 2.39 and 2.55 eV, respectively, indicating that a slight up-shift of VB top position (0.16 eV) was caused by the Co-doping modification.

In order to investigate the crystal structural changes before and after Co-doping modification, the Raman spectra of Co-BiOCl and BiOCl samples were obtained and the results are shown in Fig. 5. There are three peaks occurred at 143.6, 199.2 and 395.5 cm^{-1} for BiOCl. The 143.6 and 199.2 cm^{-1} peaks are assigned to A_{1g} and E_g inherent Bi-Cl stretching mode in BiOCl respectively, and the 395.5 cm^{-1} peak can be attributed to B_{1g} and E_g band, which originates from the motion of O atoms [33]. When it comes to Co-BiOCl, the peak at 395.5 cm^{-1} almost disappears, indicating the vibration of the local O atoms [29]. Moreover, the two peaks at 142.2 and 196.9 cm^{-1} can be attributed to A_{1g} and E_g, respectively, showing a slight blue-shift compared with that of BiOCl. The Co element was chemically coordinated with the host crystal of BiOCl and yielded the lattice of BiOCl to form the Co-BiOCl crystal [32]. Therefore, the XRD, XPS and Raman analytical results show that
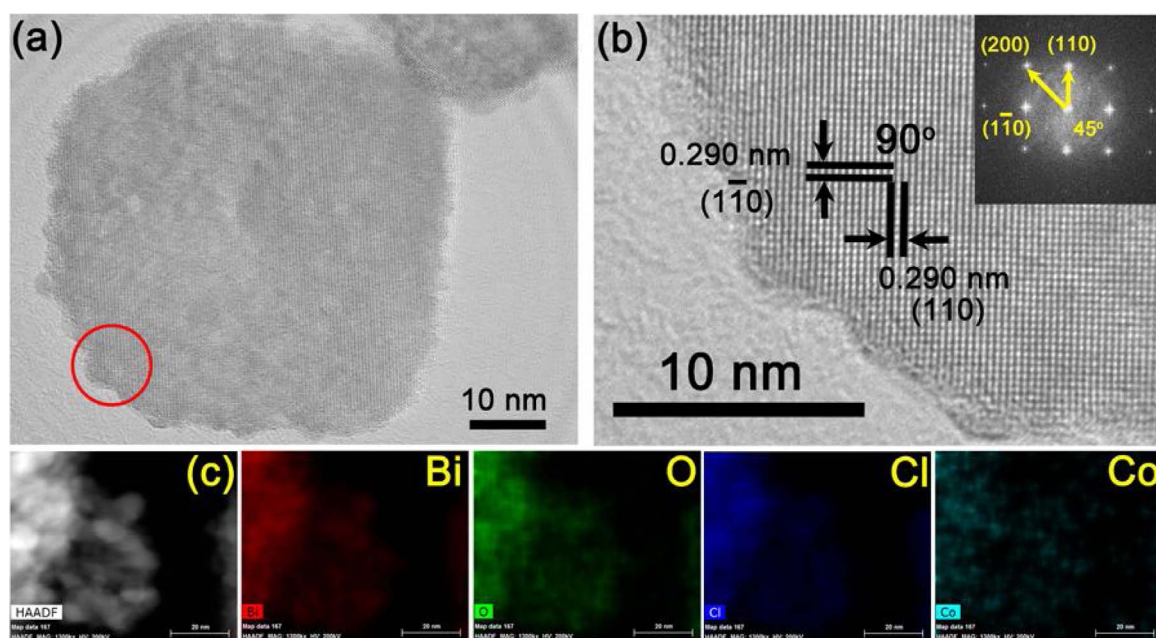

Fig. 3. (a) TEM, (b) HRTEM, and (c) STEM image and EDS mapping of the Co-BiOCl nanosheets, and the insert in (b) is the corresponding SAED pattern.
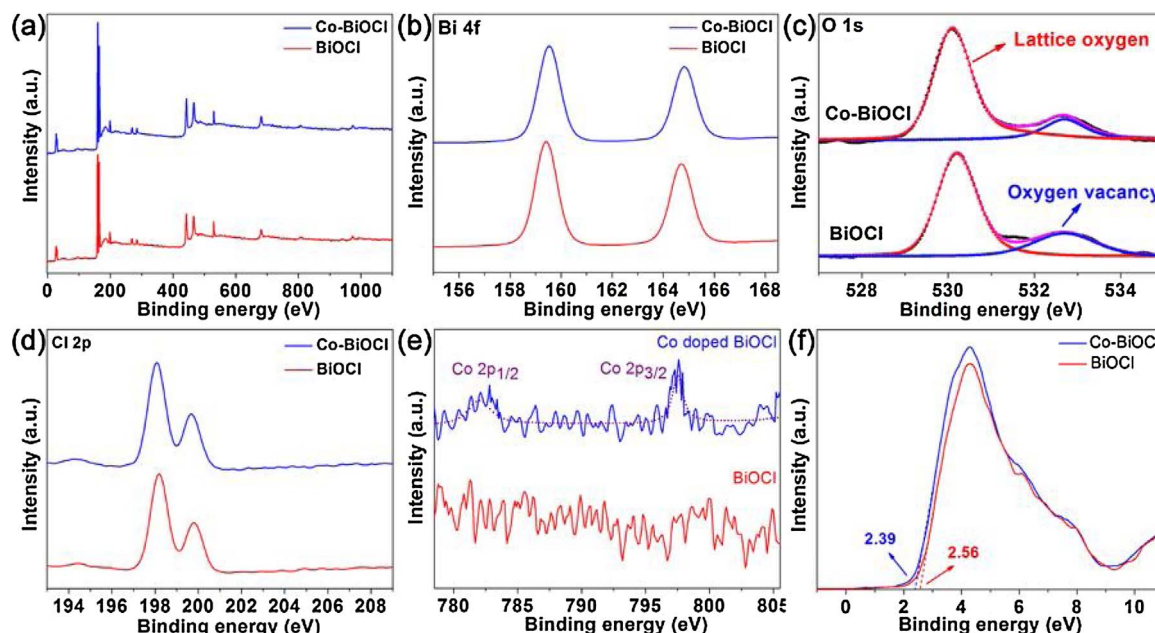
Fig. 4. (a) XPS survey spectra, (b) Bi 4f, (c) O 1s, (d) Cl 2p, (e) Co 2p, and (f) valence band spectra of the Co-BiOCl and BiOCl.
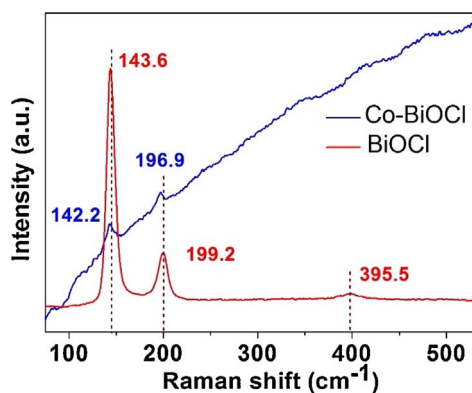

Fig. 5. Raman spectra of Co-BiOCl and BiOCl.

Co element replaced some Bi in $[Bi_2O_2]^{2+}$ layers after Co-doping modification. It is reported that there are strong covalent bindings in $[Bi_2O_2]^{2+}$ layers, but only weak nonbonding interactions (van der Waals) in $[Cl_2]^{2-}$ layers [33]. Thus, in the crystal of the as-prepared Co-BiOCl, the doped Co was in contact with O and formed Co-O bonds, rather than Co-Cl bonds. The above results of XRD, TEM, HRTEM, SAED, EDS mapping, XPS and Raman analyses demonstrate that the two-dimensional sheet-like BiOCl with the exposure of (001) facet was the main component of the as-prepared product, and a little amount of

Co was doped and bonded with O^{2-} in the layer of $[Bi_2O_2]^{2+}$.

3.2. Roles of Co-doping modification

The photocatalytic activity of a photocatalyst is determined by light absorption, charge separation and charge injection, which can be described as the following equation [9]:

$$\eta_{PC} = \eta_{LA} \times \eta_{CS} \times \eta_{CI} \tag{1}$$

where η_{PC}, η_{LA}, η_{CS} and η_{CI} are the photocatalytic activity, light absorption efficiency, charge separation efficiency and charge injection efficiency respectively.

All these aforementioned factors might be changed by the doping of other elements. Firstly, band structure is a key factor that not only directly governs the optical property but also has a great influence on the redox activity of a photocatalyst [17]. Thus, the UV-vis-NIR DRS spectra of the as-prepared Co-BiOCl and BiOCl were measured in order to obtain their band structure (Fig. 6). The UV-vis-NIR DRS spectra (Fig. 6a) show that both Co-BiOCl and BiOCl had strong absorptions in UV region, and their intrinsic optical absorption edges were similar and occurred at approximately 380 nm, indicating that both Co-BiOCl and BiOCl were UV-driven photocatalysts and had wide band gaps. On the basis of UV-vis-NIR DRS spectrum, the band gap of a semiconductor can be calculated using the following equation [40]:

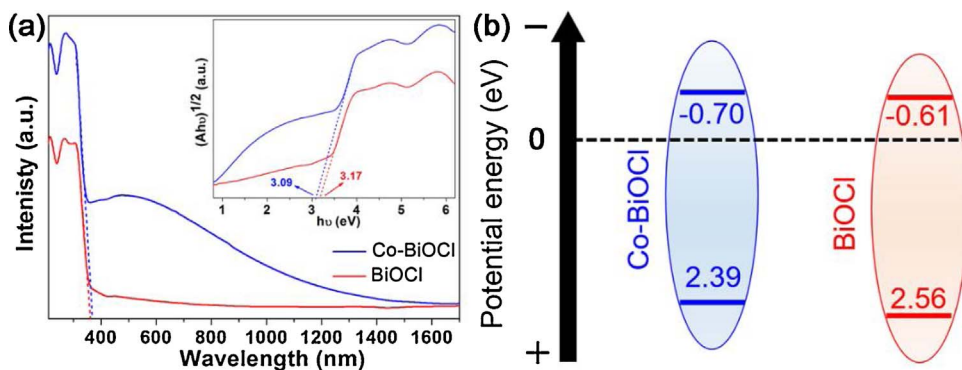$$\alpha h\upsilon = A(h\upsilon - E_g)^{n/2} \tag{2}$$

Fig. 6. (a) UV-vis-NIR DRS spectra, and the insert are the corresponding Tauc curves, and (b) band structure diagrams of the Co-BiOCl and BiOCl.

where a, $h\nu$, A and E_g, are the absorption coefficient, photon energy, a constant and the band gap, respectively. The n value is 4 here because BiOCl is a typical indirect gap semiconductor.

The calculated Tauc curves are shown in the insert of Fig. 6a. The band gap of a semiconductor is governed by the linear region, which is above the optical absorption edge. Thus, the specific band gap energies of the as-prepared Co-BiOCl and BiOCl were 3.09 and 3.17 eV, respectively. This result shows that the Co-doping modification did not substantially change the band gap of BiOCl as the amount of Co was very limited and the host crystal of the product was still BiOCl, as demonstrated by the XRD patterns in Fig. 1. Taking VB top positions into consideration (Fig. 4f), the conduction band (CB) bottom positions of the Co-BiOCl and BiOCl were calculated as −0.70 and −0.61 eV, respectively (from $E_{VB} = E_g + E_{CB}$), and the results are shown in Fig. 6b.

Nevertheless, Fig. 6a clearly shows that an additional absorption tail occurred in UV-vis-NIR DRS spectrum of the Co-BiOCl, which covered the whole visible light region. Thus, the Co-BiOCl nanosheets were able to respond towards visible light although the irradiation wavelength was larger than the absorption edge of 380 nm. It is known that the variation of structure and composition of semiconductor nanocrystals induced by doping would tailor the electronic structure and the optical absorption property. Generally, doping on the surface or in the shallow lattice of host nanocrystal generates a doping energy level in the band gap and thus causes an increased absorption of additional shoulder-like tail without changing the intrinsic optical absorption edge [33]. Since the intrinsic optical absorption edge of the Co-BiOCl nanosheets did not show an overall parallel red-shift compared to that of BiOCl, but an increased absorption tail occurred in the UV-vis-NIR DRS spectrum of the Co-BiOCl. Instead, the doped Co element concentrated on the surface or in the shallow lattice of the host crystal and formed a doping energy level in the band gap of BiOCl. Thus, the light absorption region of the Co-BiOCl nanosheets was expanded to visible light, although the Co-BiOCl still had a wide band gap of 3.09 eV.

In order to evaluate the charge separation efficiencies of the as-prepared Co-BiOCl and BiOCl, the EIS Nyquist spectra and Mott-Schottky plots were measured. The impedance of Co-BiOCl nanosheets was much lower than that of BiOCl, which was confirmed by the smaller curvature radius in the EIS Nyquist spectra (Fig. 7a), indicating

that the doped Co element remarkably enhanced the charge transportation efficiency of BiOCl. On the other hand, the intrinsic charge carrier density (N_d) can be calculated from the slope of Mott-Schottky plots with the following equation [40]:

$$N_d = (2/e_0 \varepsilon \varepsilon_0)[d(C^{-2})/dV]^{-1} \quad (3)$$

where e_0 is the electron charge, ε and ε_0 are the dielectric constant of the sample and the permittivity of the vacuum respectively, and $d(C^{-2})/dV$ is the slope of the liner part in the Mott-Schottky plot. Therefore, the intrinsic charge carrier density is reciprocal with the slope of the liner part in the Mott-Schottky plot.

The Mott-Schottky plots reveal that the slop of Co-BiOCl was a slightly smaller than that of BiOCl, which is fitted by dashed lines in Fig. 7b, indicating that the doped Co element slightly enhanced the intrinsic charge carrier density of BiOCl. The EIS and Mott-Schottky tests show that the Co-doping modification not only enhanced the intrinsic charge carrier density, but also enhanced the charge transportation efficiency, resulting in a higher efficiency of charge separation in the Co-BiOCl nanosheets.

Series of photocurrent tests were carried out to explore the charge injection properties of Co-BiOCl and BiOCl, and UV light was used in order to make a fair comparison between the Co-BiOCl and BiOCl as BiOCl was insensitive towards visible light. In UV region, the light absorption efficiency of the Co-BiOCl was 1.7 times higher than that of the BiOCl, as revealed by the UV-vis-NIR DRS spectra (Fig. 6a). Since the light absorption efficiency (η_{LA}) was known, and the photocurrent density was proportional to the photocatalytic activity, Eq. (1) could be simplified as follows:

$$I^{UV} = \eta_{CS} \times \eta_{CI} \quad (4)$$

where I^{UV} is the photocurrent density under UV light irradiation. The photocurrent densities of the Co-BiOCl and BiOCl were measured (Fig. 7c). Both Co-BiOCl and BiOCl exhibited photocurrent responses toward UV light, but the stabilized response intensity of the Co-BiOCl was 3.2 times higher than that of the BiOCl, which is shown in Eq. (5):

$$I^{UV}(Co\text{-}BiOCl)/I^{UV}(BiOCl) = 3.2 \quad (5)$$

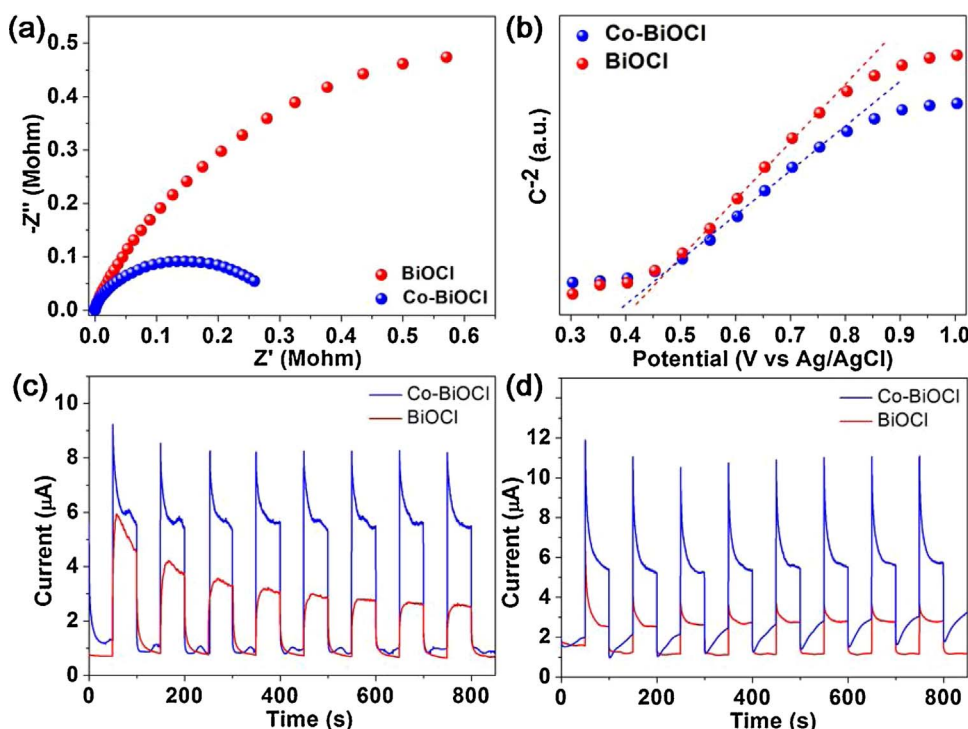When $K_2S_2O_8$ (noted as KSO) was used as the scavenger of

Fig. 7. (a) EIS Nyquist spectra, (b) Mott-Schottky plots, and photocurrent responses in the aqueous solution containing (c) only Na_2SO_4 and (d) Na_2SO_4 and $K_2S_2O_8$ of the Co-BiOCl and BiOCl, respectively.

photogenerated e[−], the charge injection efficiency could be eliminated ($\eta_{CI}^{KSO} = 1$) [9], and Eq. (4) was further simplified as follows:

$$I^{UV+KSO} = \eta_{CS} \tag{6}$$

where I^{UV+KSO} is the photocurrent density under UV light irradiation with the presence of $K_2S_2O_8$.

The corresponding results are shown in Fig. 7d, and the stabilized response intensity of the Co-BiOCl was approximately 3.3 times higher than that of the BiOCl, which is shown in Eq. (7):

$$I^{UV+KSO}(\text{Co-BiOCl})/I^{UV+KSO}(\text{BiOCl}) = 3.3 \tag{7}$$

Since the light absorption efficiency of the Co-BiOCl was 1.7 times higher than that of the BiOCl, the charge separation efficiency of the former was estimated as 1.9 times higher than that of the latter. On the other hand, a comparison between Eq. (1) with Eq. (7) indicates that the utilization of $K_2S_2O_8$ did not substantially change the ratio of photocurrent response intensities of the Co-BiOCl and BiOCl, which is shown below:

$$I^{UV+KSO}(\text{Co-BiOCl})/I^{UV+KSO}(\text{BiOCl}) = I^{UV}(\text{Co-BiOCl})/I^{UV}(\text{BiOCl}) \tag{8}$$

Namely,

$$\frac{\eta_{CS}(\text{Co}-\text{BiOCl})}{\eta_{CS}(\text{BiOCl})} = \frac{\eta_{CS}(\text{Co}-\text{BiOCl}) \times \eta_{CI}(\text{Co}-\text{BiOCl})}{\eta_{CS}(\text{BiOCl}) \times \eta_{CI}(\text{BiOCl})} \tag{9}$$

Thus,

$$\eta_{CI}(\text{Co-BiOCl}) = \eta_{CI}(\text{BiOCl}) \tag{10}$$

The above result shows that the charge injection efficiency of the Co-BiOCl was not enhanced and the doped Co element was not an extra channel for the injection of photogenerated e[−] into the adsorbed molecule. The doped Co element on the surface or in the shallow lattice of BiOCl formed an additional doping energy level and remarkably expanded the light absorption range into visible light region. The electrons in the VB of the Co-BiOCl nanosheets were firstly transited into the Co doping energy level by the interconversion between Co^{2+} and Co^{3+}, then excited by visible light irradiation and finally injected to the CB [32]. Furthermore, the doped Co element substantially enhanced the charge separation efficiency of BiOCl by approximately 1.9 times. These results suggest that the as-prepared Co-BiOCl nanosheets might possess an outstanding photocatalytic performance under visible light irradiation.

3.3. Photocatalytic degradation of BPA by Co-BiOCl nanosheets

In order to evaluate the photocatalytic performance of the Co-BiOCl nanosheets, BPA was chosen as the target pollutant because it was colorless and thus the impact of dye-sensitization could be eliminated. The experiments of BPA degradation under visible light irradiation using the Co-BiOCl, BiOCl and TiO$_2$ (P25) as photocatalysts are shown in Fig. 8a. The blank test revealed that BPA was stable in the absence of photocatalysts under visible light irradiation. After 120-min irradiation,

only approximately 10% of BPA was degraded by TiO$_2$ (P25), which resulted from its wide band gap and insensitivities of visible light. It is worth noting that about 20% of BPA was degraded by BiOCl because the light absorption region could be broadened slightly by oxygen vacancy in the crystal of BiOCl. However, the Co-BiOCl nanosheets exhibited a much better performance than TiO$_2$ (P25) and BiOCl, and more than 95% of BPA was degraded under visible light irradiation within 120 min. Moreover, more than 90% of the photocatalytic activity of the Co-BiOCl nanosheets retained after 5 cycles (Fig. S4), and the molar ratio of Co:Bi of the tested sample was still 1:85, indicating the good stability of the Co-BiOCl nanosheets. In order to optimize the amount of doped Co, a series of Co-BiOCl samples with different amounts of doped Co by changing the dosage of CoCl$_2$ were prepared. Their performances for the photocatalytic degradation of BPA under visible light irradiation were investigated (Table S1 and Fig. S5). The result shows that the sample of 0.1 mmol CoCl$_2$ exhibited the best performance.

To quantitatively compare the photocatalytic activities of the Co-BiOCl nanosheets, TiO$_2$ (P25) and BiOCl, the corresponding kinetic constants were calculated by fitting the experimental degradation curves to the Langmuir-Hinshelwood model. Since the reactant concentration was low, the pseudo first-order kinetics equation was used [17]:

$$-\ln(C_t/C_0) = kt \tag{11}$$

where C_t is the concentration of BPA at a specific time t, C_0 is the original concentration, and k is the kinetic constant.

As is shown in Fig. 8b, the kinetic curves were fitted well by the pseudo first-order kinetic model with high correlation coefficients. The calculated k values were 0.021 and 0.003 min^{-1} for the Co-BiOCl, and BiOCl, respectively, and the k values of TiO$_2$ (P25) and blank test were negligible, indicating that the apparent photocatalytic activity of the Co-BiOCl was 7 times higher than that of the BiOCl. When the differences in active sites exposure were eliminated, the surface-area-normalized kinetic constants were 1.23 and 0.35 mg m^{-2} min^{-1} for the Co-BiOCl, and BiOCl respectively. Thus, the intrinsic photocatalytic activity of the Co-BiOCl was approximately 3.5 times higher than that of the BiOCl.

The efficiency of photocatalytic degradation relies greatly on the oxidizability of photogenerated h[+] and the amount of produced reactive oxygen species (ROS) in the photocatalytic reaction [17]. ESR and fluorescence tests were conducted to investigate the ROS ($\cdot O_2^-$, $\cdot OOH$ and $\cdot OH$) produced by the Co-BiOCl and BiOCl (Fig. S6). In the ESR tests, the four peaks with the same intensity (Fig. S6a) and the seven peaks with the intensity of 1:2:1:2:1:2:1 (Fig. S6b) were the characteristic signals of $\cdot O_2^-$ and $\cdot OOH$ respectively. Thus, the Co-BiOCl nanosheets were able to produce large quantities of $\cdot O_2^-$ and $\cdot OOH$ under visible light irradiation. However, no signals occurred when the BiOCl was tested because it possessed a wide band gap and had no response towards visible light. Furthermore, the generated $\cdot OH$ can be trapped by terephthalic acid (TPA) and then form TPA$\cdot$OH, which
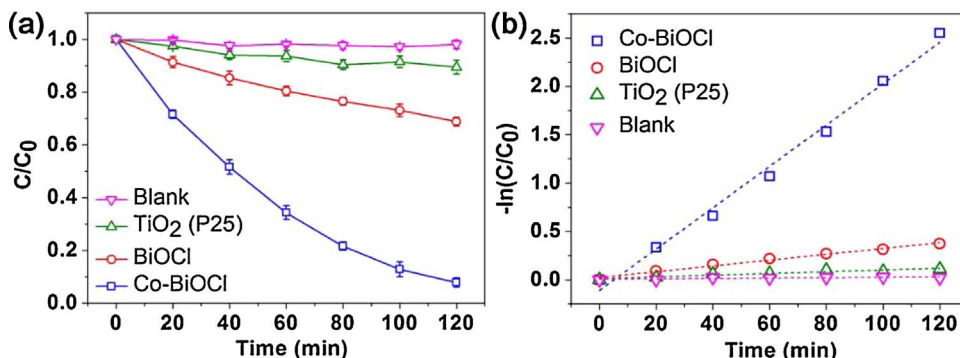

Fig. 8. (a) Photocatalytic degradation curves, and (b) corresponding kinetic curves of the Co-BiOCl and BiOCl, respectively.
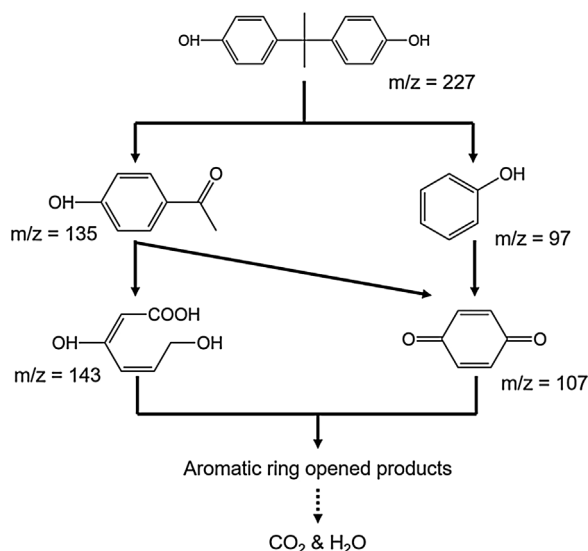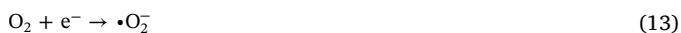
Fig. 9. Photocatalytic degradation pathway of BPA.

possesses a characteristic fluorescence emission signal at the wavelength of 420 nm [40]. Obviously, the fluorescence emission intensity of the Co-BiOCl was enhanced (**Fig. S6c**), but that of BiOCl showed no substantial changes (**Fig. S6d**), indicating that only the Co-BiOCl nanosheets were able to produce ·OH under visible light irradiation. Since the VB top position of Co-BiOCl (2.39 eV) is more positive than that of OH$^-$/·OH (2.3 eV), ·OH is generated by both h$^+$ on VB and e$^-$ on CB as follows [17]:

$$h^+ + H_2O \rightarrow \cdot OH + H^+ \qquad (12)$$

$$O_2 + e^- \rightarrow \cdot O_2^- \qquad (13)$$

$$\cdot O_2^- + H_2O \rightarrow \cdot OOH + OH^- \qquad (14)$$

$$\cdot OOH + 2e^- + H_2O \rightarrow \cdot OH + 2OH^- \qquad (15)$$

In order to test the roles of the active species responsible for the BPA degradation, various scavengers, such as sodium oxalate ($Na_2C_2O_4$) for h$^+$, tert-butyl alcohol (TBA) for ·OH, p-benzoquinone (PBQ) for ·O$_2^-$ and N$_2$-purging for molecular oxygen, were used [17]. The BPA degradation was substantially suppressed by the dose of $Na_2C_2O_4$, and non-negligible suppressions also occurred when TBA, PBQ and N$_2$-purging were used, indicating that the contribution of each active species was in the order of h$^+$ > ·O$_2^-$ > ·OH (**Fig. S7a**). Thus, the photogenerated h$^+$ was the main active species responsible for the BPA

degradation under visible light irradiation, and the contribution of h$^+$ was calculated as 85% with the kinetic constants in **Fig. S7b**.

The generated intermediates in the BPA degradation were detected using a GC-MS, and four intermediates were identified (Fig. 9) [17,21]. The ion at m/z 227 represented BPA. There were two main product ions at m/z 135 and 97, which were identified as p-hydroxyacetophenone and phenol, respectively. Thus, the BPA was mainly split at the quaternary carbon atom between two benzene rings, and then transformed into the two intermediates. After that, the intermediates were further oxidized by the reactive species and converted into p-benzoquinone (m/z 107). Meanwhile, p-hydroxyacetophenone was partially oxidized more violently with a direct cleaving of aromatic rings, and transformed into the intermediate of m/z 143. Then, these degradation products reacted with the reactive species and were finally mineralized into CO_2 and H_2O after sufficient irradiation time.

3.4. Mechanisms behind the enhanced visible-light-driven photocatalytic performance of Co-BiOCl nanobelts

To further understand the influening mechanism of Co doping on electronic structures of BiOCl nanosheets at atomic and electronic levels, first-principles calculations were performed for the (001) facet of BiOCl before and after Co doping modification to obtain their electronic energy band structures and densities of states (DOS) (Fig. 10) as well as the corresponding projected DOS (PDOS) in **Fig. S8**. The results show that the intrinsic positions of the VB and CB almost remained unchanged after Co-doping modification. However, an additional energy level appeared as the mid-gap state in the band gap of Co-BiOCl, which was mainly contributed by Co 3d orbitals and a little O 2p orbitals. With the measured VB maximum (2.39 eV) and CB minimum (-0.70 eV), the position of Co doping energy level was calculated to be 1.19 eV. This result demonstrates that the doped Co was bound with O to form Co-O bonds in [Bi$_2$O$_2$]$^{2+}$ layers. In this way, the doped Co induced O 2p orbitals to compose the doping energy level in the band gap of BiOCl to promote the photogenerated electron-hole separation, and thus substantially enhanced the visible-light-driven photocatalytic performance.

3.5. Photocatalytic mechanism of BPA degradation over Co-BiOCl nanosheets

On the basis of the aforementioned results, the photocatalytic BPA degradation process with the as-prepared Co-BiOCl nanosheets under visible light irradiation was elucidated and illustrated in Fig. 11. First, the electrons in the VB of the Co-BiOCl nanosheets were transited into the Co doping energy level by the interconversion between Co^{2+} and Co^{3+}. Then, the electrons in the Co doping energy level was excited by
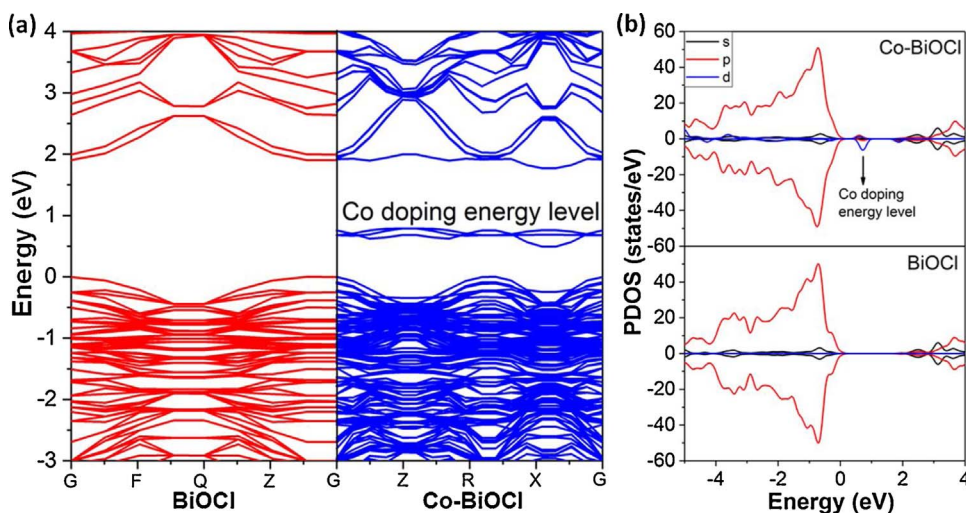

Fig. 10. (a) Calculated electronic energy band structures and (b) DOS of BiOCl and Co-BiOCl.
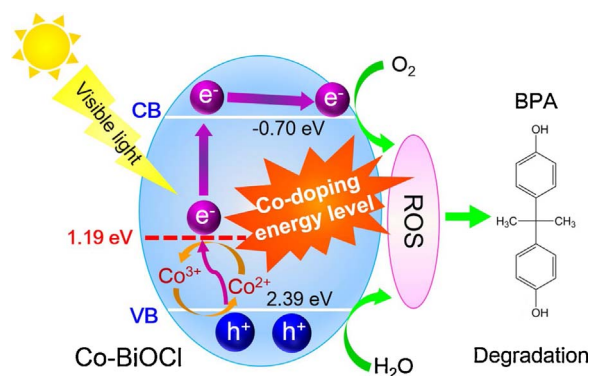
Fig. 11. Schematic of BPA degradation over Co-BiOCl nanosheets.

visible light irradiation and injected to the CB of the Co-BiOCl nanosheets. After that, photogenerted h^+ and e^- reacted with H_2O and dissolved O_2 respectively, forming various ROS. Finally, the generated ROS and a part of h^+ reacted with BPA to complete the degradation process.

4. Conclusions

In this work, Co-BiOCl nanosheets were obtained using a simple hydrothermal route without additional treatments. The doped Co element on the surface or in the shallow lattice of the host crystal substantially enhanced the intrinsic photocatalytic activity of BiOCl from two aspects, i.e., forming a doping energy level in the band gap and enhancing the charge transportation efficiency. As a result, the as-prepared Co-BiOCl nanosheets exhibited a strong response towards visible light and possessed a high efficiency of charge separation. Thus, the Co-BiOCl nanosheets exhibited an outstanding performance for BPA degradation under visible light irradiation with a degradation rate of 3.5 times higher than that of BiOCl. The DFT calculation results further confirmed the aforementioned mechanism. Moreover, the good stability of the Co-BiOCl nanosheets was also confirmed. The photogenerated h^+ was found to be the main active species for the photocatalytic BPA degradation. This work not only shows a promising application of the Co-BiOCl nanosheets in the visible-light driven photocatalytic degradation of pollutants, but also provided a new strategy for the design and synthesis of high-performance visible light sensitive photocatalysts.

Acknowledgments

Appendix A. Supplementary data

Supplementary data associated with this article can be found, in the online version, at http://dx.doi.org/10.1016/j.apcatb.2017.09.036.

References

[1] R. Li, H. Han, F. Zhang, D. Wang, C. Li, Energy Environ. Sci. 7 (2014) 1369–1376.
[2] W. Wang, X. Huang, S. Wu, Y. Zhou, L. Wang, H. Shi, Y. Liang, B. Zou, Appl. Catal. B: Environ. 134–135 (2013) 293–301.
[3] S. Wang, X. Hai, X. Ding, K. Chang, Y. Xiang, X. Meng, Z. Yang, H. Chen, J. Ye, Adv. Mater (2017) 1701774–1701780.
[4] H. Gnayem, Y. Sasson, ACS Catal. 3 (2013) 186–191.
[5] L. Ye, Y. Su, X. Jin, H. Xie, C. Zhang, Environ. Sci.: Nano 1 (2014) 90–112.
[6] J. Li, H. Li, G. Zhan, L. Zhang, Acc. Chem. Res. 50 (2017) 112–121.
[7] J. Li, Y. Yu, L. Zhang, Nanoscale 6 (2014) 8473–8488.
[8] A.M. Ganose, M. Cuff, K.T. Butler, A. Walsh, D.O. Scanlon, Chem. Mater. 28 (2016) 1980–1984.
[9] L. Sun, L. Xiang, X. Zhao, C.-J. Jia, J. Yang, Z. Jin, X. Cheng, W. Fan, ACS Catalysis 5 (2015) 3540–3551.
[10] J. Li, L. Cai, J. Shang, Y. Yu, L. Zhang, Adv. Mater. 28 (2016) 4059–4064.
[11] S. Wu, J. Xiong, J. Sun, Z.D. Hood, W. Zeng, Z. Yang, L. Gu, X. Zhang, S.Z. Yang, ACS Appl. Mater. Interfaces 9 (2017) 16620–16626.
[12] F. Tian, Y. Zhang, G. Li, Y. Liu, R. Chen, New J. Chem. 39 (2015) 1274–1280.
[13] K. Li, Y. Tang, Y. Xu, Y. Wang, Y. Huo, H. Li, J. Jia, Appl. Catal. B: Environ. 140–141 (2013) 179–188.
[14] N. Barbero, D. Vione, Environ. Sci. Technol. 50 (2016) 2130–2131.
[15] X. Zhang, L.W. Wang, C.Y. Wang, W.K. Wang, Y.L. Chen, Y.X. Huang, W.W. Li, Y.J. Feng, H.Q. Yu, J. Chem Eur, 21 (2015) 11872–11877.
[16] C.Y. Wang, X. Zhang, X.N. Song, W.K. Wang, H.Q. Yu, ACS Appl. Mater. Interfaces 8 (2016) 5320–5326.
[17] C.Y. Wang, X. Zhang, H.B. Qiu, W.K. Wang, G.X. Huang, J. Jiang, H.Q. Yu, Appl. Catal. B: Environ. 200 (2017) 659–665.
[18] M. Guan, C. Xiao, J. Zhang, S. Fan, R. An, Q. Cheng, J. Xie, M. Zhou, B. Ye, Y. Xie, J. Am. Chem. Soc. 135 (2013) 10411–10417.
[19] F. Dong, Q. Li, Y. Sun, W.-K. Ho, ACS Catal. 4 (2014) 4341–4350.
[20] H. Li, J. Shang, H. Zhu, Z. Yang, Z. Ai, L. Zhang, ACS Catal. 6 (2016) 8276–8285.
[21] M. Pan, H. Zhang, G. Gao, L. Liu, W. Chen, Environ. Sci. Technol. 49 (2015) 6240–6248.
[22] H. Li, J. Shang, Z. Yang, W. Shen, Z. Ai, L. Zhang, Environ. Sci. Technol. 51 (2017) 5685–5694.
[23] J. Di, J. Xia, M. Ji, B. Wang, S. Yin, Y. Huang, Z. Chen, H. Li, Appl. Catal. B: Environ. 188 (2016) 376–387.
[24] J. Di, J. Xia, M. Ji, B. Wang, S. Yin, Q. Zhang, Z. Chen, H. Li, Appl. Catal. B: Environ. 183 (2016) 254–262.
[25] L. Zhang, Z. Han, W. Wang, X. Li, Y. Su, D. Jiang, X. Lei, S. Sun, Chemistry 21 (2015) 18089–18094.
[26] X. Chang, S. Wang, Q. Qi, M.A. Gondal, S.G. Rashid, D. Yang, M.A. Dastageer, K. Shen, Q. Xu, P. Wang, Appl. Catal. B: Environ. 176–177 (2015) 201–211.
[27] X. Xiao, C. Liu, R. Hu, X. Zuo, J. Nan, L. Li, L. Wang, J. Mater. Chem. 22 (2012) 22840–22843.
[28] N. Yu, Y. Chen, W. Zhang, M. Wen, L. Zhang, Z. Chen, Mater. Lett. 179 (2016) 154–157.
[29] C. Huang, J. Hu, S. Cong, Z. Zhao, X. Qiu, Appl. Catal. B: Environ. 174–175 (2015) 105–112.
[30] H. Fujito, H. Kunioku, D. Kato, H. Suzuki, M. Higashi, H. Kageyama, R. Abe, J. Am. Chem. Soc. 138 (2016) 2082–2085.
[31] D. Wu, S. Yue, W. Wang, T. An, G. Li, H.Y. Yip, H. Zhao, P.K. Wong, Appl. Catal. B: Environ. 192 (2016) 35–45.
[32] Y. Mi, L. Wen, Z. Wang, D. Cao, R. Xu, Y. Fang, Y. Zhou, Y. Lei, Nano Energy 30 (2016) 109–117.
[33] J. Li, K. Zhao, Y. Yu, L. Zhang, Adv. Funct. Mater. 25 (2015) 2189–2201.
[34] Z. Wu, J. Wang, L. Han, R. Lin, H. Liu, H.L. Xin, D. Wang, Nanoscale 8 (2016) 4681–4687.
[35] X. Xu, C. Su, W. Zhou, Y. Zhu, Y. Chen, Z. Shao, Adv. Sci. 3 (2016) 1500187–1500192.
[36] J. Staszak-Jirkovsky, C.D. Malliakas, P.P. Lopes, N. Danilovic, S.S. Kota, K.C. Chang, B. Genorio, D. Strmcnik, V.R. Stamenkovic, M.G. Kanatzidis, N.M. Markovic, Nat. Mater. 15 (2016) 197–203.
[37] J. Xiong, G. Cheng, G. Li, F. Qin, R. Chen, RSC Adv. 1 (2011) 1542–1553.
[38] M.D. Segall, P.J.D. Lindan, M.J. Probert, C.J. Pickard, P.J. Hasnip, S.J. Clark, M.C. Payne, J. Phys.: Condens. Matter. 14 (2002) 2717–2744.
[39] J.P. Perdew, K. Burke, M. Ernzerhof, Phys. Rev. Lett. 77 (1996) 3865–3868.
[40] C.Y. Wang, X. Zhang, H.B. Qiu, G.X. Huang, H.Q. Yu, Appl. Catal. B: Environ. 205 (2017) 615–623.
[41] N. Zhang, X. Li, H. Ye, S. Chen, H. Ju, D. Liu, Y. Lin, W. Ye, C. Wang, Q. Xu, J. Zhu, L. Song, J. Jiang, Y. Xiong, J. Am. Chem. Soc. 138 (2016) 8928–8935.
[42] C. Meng, T. Ling, T.Y. Ma, H. Wang, Z. Hu, Y. Zhou, J. Mao, X.W. Du, M. Jaroniec, S.Z. Qiao, Adv. Mater. 29 (2017) 1604607–1604613.
[43] Y. Liang, Y. Li, H. Wang, J. Zhou, J. Wang, T. Regier, H. Dai, Nat. Mater. 10 (2011) 780–786.